Time-Domain Electromagnetic Characterization of Reaction Wheel for Space Applications

Marc Pous ⬤, *Member, IEEE*, Dongsheng Zhao ⬤, *Senior Member, IEEE*,
Marco A. Azpúrua ⬤, *Senior Member, IEEE*, Teodor Bozhanov ⬤, *Member, IEEE*,
Ferran Silva ⬤, *Senior Member, IEEE*, and Johannes Wolf, *Senior Member, IEEE*

Abstract—**The electromagnetic characterization of reaction wheels is crucial to comply with the demanding ac magnetic field cleanliness requirements of space science missions, thus, preventing interference on sensitive onboard instrumentation. Therefore, a complete assessment, including the measurement of the magnetic flux vector at different operational modes and under dynamic conditions, is proposed as a contribution beyond conventional testing methodologies. This article investigates the worst-case magnetic field emissions experimentally, using a test setup based on a multi-channel acquisition and multidomain postprocessing system. The focus of the measurement campaign was on the low-frequency range (10 Hz–2 kHz). Moreover, capturing the B-field in the time-domain enabled further analysis, that is, complementary outputs for understanding the electromagnetic performance of the reaction wheel. As a result, we can relate the wheel rotation with the current and the magnetic fields, compute the field orientation, and evaluate in-band interference for the magnetic field.**

Index Terms—**Aerospace, electromagnetic interference, magnetic field emissions, reaction wheel, time-domain measurements.**

I. INTRODUCTION

THE electromagnetic characterization of a reaction wheel is critical for aerospace applications. The reaction wheels have already been used for decades to provide precise control and pointing accuracy. Nevertheless, improving reaction wheels' technology and performance can be challenging from an electromagnetic compatibility (EMC) point of view. The reaction wheel, which is driven by electric currents, is composed of a rotor, a stator, and a flywheel. The motor originates a rotation on the flywheel producing an angular momentum compensated by a motion in the opposite direction, moving the spacecraft. Controlling electromagnetic interference (EMI) is even more important as recent space scientific missions require lower levels of magnetic field emissions to conduct experiments onboard [1], [2], [3], [4], [5], [6]. In fact, reaction wheels can compromise scientific data, and sometimes, results have to be discarded.

Regarding the possible sources of EMI, different primary magnetic field emissions are produced by the reaction wheel. The magnetostatic contributions are due to the properties of the materials used, including the magnets necessary for the motor, and the magnetic field generated by the dc current driving the motors [7], [8]. In contrast, the ac magnetic field disturbances are consequence of the rotation of the magnets inside the motor, the magnetization of the flywheel employing materials like steel, as well as potentially noisy current flowing through windings used to drive the motor. Hence, the reaction wheel's speed and current consumption produce time-varying emissions that shall be evaluated to find out the worst case under dynamic operating conditions. This aspect makes conventional testing methods based on the frequency sweep technique not effective to unveil plausible EMC problems. Accordingly, the detailed and in-depth electromagnetic characterization of such complex and critical component is key to improve aerospace systems reliability.

Recently, multichannel time-domain methods have been developed to evaluate complex EMI scenarios. Such techniques provide an agile approach to overcome several challenges arising in EMC assessments, e.g., finding the worst case for time-varying interference, defining adequate dwell times, or correlating the operating mode of the equipment under test (EUT) with its electromagnetic emissions [9]. For instance, in [10], EMI caused by the dynamic mode of a rolling stock was characterized by employing time-domain captures. This work demonstrated the feasibility of catching the worst-case of short-duration events, increasing the measurement time at each frequency up to 2500 times for specific bands.

In opposition to the typical swept EMI receiver, transient or time-varying events can be detected and acquired using instrumentation with a real-time, direct sampling, architecture. Moreover, the possibility of measuring complementary inputs

Marc Pous is with the Electromagnetic Compatibility Group (GCEM), Universitat Politécnica de Catalunya, 08034 Barcelona, Spain, and also with the European Space Agency, ESTEC, 7501263 Noordwijk, The Netherlands (e-mail: marc.pous@upc.edu).

Dongsheng Zhao, Teodor Bozhanov, and Johannes Wolf are with the European Space Agency, ESTEC, 7501263 Noordwijk, The Netherlands (e-mail: dongsheng.zhao@esa.int; teodor.bozhanov@esa.int; johannes.wolf@esa.int).

Marco A. Azpúrua is with the EMC Electromagnetic BCN S.L. (EMC Barcelona), 08034 Barcelona, Spain, and also with the Universitat Politécnica de Catalunya, 08034, Barcelona, Spain (e-mail: marco.azpurua@upc.edu).

Ferran Silva is with the Electromagnetic Compatibility Group (GCEM), Universitat Politécnica de Catalunya, 08034 Barcelona, Spain (e-mail: ferran.silva@upc.edu).

synchronously allows to correlate emission and events from different operating modes, even if they have short duration [11]. This multichannel approach is helpful for coping with measurements in the presence of background noise like those related to mains frequency and its harmonics that can mask the actual emissions from the EUT.

In this work, we perform a tailor-made, multidomain characterization of the magnetic field emissions of a reaction wheel using multichannel time-domain measurements for providing a more comprehensive assessment of EMI in the low-frequency range. The investigation is carried out experimentally. Representative operating modes are defined to characterize the EUT under dynamic conditions, including acceleration, deceleration, and short-time speed modification states.

The rest of this article is organized as follows. Section II presents the proposed methodology. Section III is devoted to describe the experiment while Section IV presents and discusses the results obtained for a reaction wheel considered for several European Space Agency (ESA) missions, manufactured by Microsat Systems Canada Inc. Finally, Section V concludes this article.

II. METHODOLOGY

This section describes the key elements of the proposed methodology, that is, the multichannel time-domain measurement system, the test setup, and the time-domain in-band postprocessing used as part of the analysis of results. The methodology was tailor made based on specific considerations and requirements from the EUT. In that sense, the study focused on the magnetic field produced by the reaction wheel mechanism's movement, and its associated source current and harmonics.

A. Multichannel Time-Domain EMI Measurement Systems

Multichannel time-domain EMI measurement and processing systems have been developed for tackling the electromagnetic emissions characterization of complex systems [10], [12]. Complex systems have time-varying, nonstationary behavior, and several different operating modes that are triggered during the EUT's normal functioning. In such systems, the EMI signature of the EUT varies during the emissions measurement. Therefore, in those conditions, the conventional EMI measurement procedures, based on the frequency-swept technique, are likely to deliver erroneous or misleading results. Furthermore, given the characteristics of the reaction wheel, it is considered a complex system from an EMC perspective.

In order to cope with the challenges mentioned above, state-of-the-art EMI receivers with multidomain and multichannel capabilities can be used (see Fig. 1). Multidomain means EMI measurements are processed and analyzed in time, frequency, and statistical domains, either independently or simultaneously. This allows for accurate spectral estimations according to standard specification [11], [13], [14] and complementary analysis, including waveform measurements, spectrograms, waterfall/persistence plots, and probabilistic information about the interference, e.g., the amplitude probability distribution (APD). Moreover, multichannel means the measurement system has more than one input. Therefore, it can perform the acquisitions
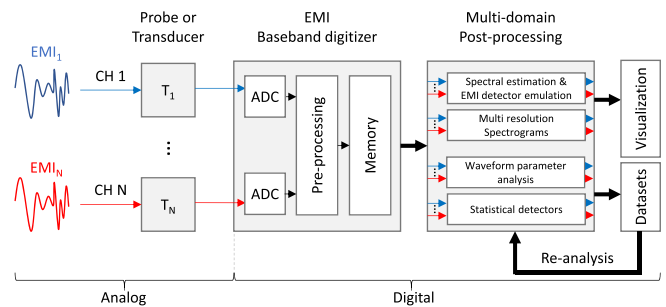

Fig. 1.   Block diagram of the multichannel time-domain EMI measurement system used during the experiments.

synchronously once a specific triggering condition/event occurs. Those further measurement and analysis capabilities beyond the standard EMC testing requirement have proven to be highly valuable for EMI assessment of complex systems [15], [16].

We used a multichannel time-domain EMI measurement system developed by GCEM-UPC that employs flexible resolution deep memory oscilloscopes to capture and process EMI waveforms. The Welch's method is used for spectral estimation along with adaptive windowing functions for setting any required resolution bandwidth. Here, the hardware used was the 4-channels USB oscilloscope model PicoScope 5444B from Pico Technology. It has up to 16-b vertical resolution, 1 GS/s of maximum sampling rate, 200 MHz bandwidth, and memory of 512 MS. With this configuration, CISPR 16-1-1 baseline requirements are met for CISPR bands A and B [13], [17]. Using the appropriate settings, it is possible to measure and record the EMI in real-time and during long time intervals. This, along with the capacity of triggering measurements according to worst-case conditions and transient events, increases the chances of identifying low-probability occurrence electromagnetic disturbances.

The short-time Fourier transform was used to produce spectrograms, that is, a representation of the time-frequency behavior of the emissions. Likewise, the spectrum was calculated using different bandwidths and frequency steps. This is useful to play with the spectrum resolution, thus resolving frequency components very close to each other, reaching a resolution bandwidth as low as 0.1 Hz for the settings above. The key parameter to obtain an equivalent resolution bandwidth when computing the FFT is to select a proper window length, considering the sampling rate. The relation is described by

$$N = f_s \frac{w_f}{RBW} \qquad (1)$$

where N is the number of samples per window, f_s is the sampling rate, w_f is the window factor, and RBW is the equivalent resolution bandwidth (RBW) obtained. The window selected to compute the spectrum is the Kaiser–Bessel, with a window factor of 3.12 and an overlapping factor of 80%, as it is optimal regarding amplitude and spectral accuracy [18].

B. Setup

The test setup is shown schematically in Fig. 2. It uses four channels of the measurement instrument in parallel. Three of them are dedicated for the B-field measurement at the proximity
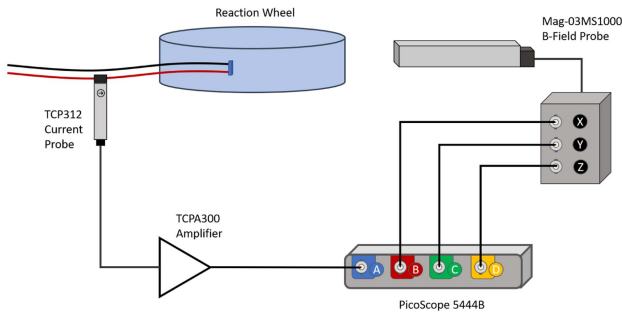
Fig. 2. Measurement setup schematic.

of the EUT. The remaining channel one was used to measure the current driving the reaction wheel.

The B-field is sensed using the Mag-03MS1000 probe from Bartington Instruments, which provides the three Cartesian components of the magnetic flux vector separately. The field probe bandwidth is limited to 2 kHz, sufficient to measure the emissions related to the reaction wheel movement, it has a noise level of $8.8\ \mathrm{pT}/\sqrt{\mathrm{Hz}}$, and the orthogonality error is lower than $0.1°$ for each component. The distance between the probe and the EUT is set to 20 cm. The x-, y-, and z- components of the probe are connected to the oscilloscope's channels B, C, and D, respectively, as represented in Fig. 2. The current probe Tektronix model TCP312 in combination with the TCPA300 amplifier, have been placed at the positive line of the reaction wheel power port. The bandwidth of this current probe is 100 MHz, and the current probe is connected to the oscilloscope channel A. For the current study, the bandwidth of the current probe is sufficient because we will measure up to 200 kHz, which is enough to observe dc/dc converter's main contribution. Nevertheless, the methodology can be extended, considering the limitations of the maximum frequency of the different probes or the oscilloscope employed. For instance, measurements have been conducted up to 1 GHz in other applications with an oscilloscope [10].

The trigger condition is set to the channel A, because it is of interest to relate events on the power port with the B-field measured through the remaining channels. Since the current probe has a broader frequency response, it will be necessary to use a sampling rate high enough to avoid aliasing errors. Hence, the sampling rate was set to 1 MSa/s, well above the Nyquist criterion. Oversampling the B-field waveforms enable resolution enhancement through digital filtering, lowering the measurement noise level due to a higher number of effective bits of the oscilloscope analogue to digital converter (ADC) resolution.

Triggering measurements with those signals from the B-field sensor output is not convenient. This is because the probe broadband response picks up field contributions from sources other than the EUT, including the unavoidable magnetic field present in the environment. From such ambient noise, the 50 Hz contribution to the B-field (and its harmonics) are dominant in terms of their amplitude. In consequence, the EUT emissions remain masked in time-domain, making it difficult to identify them without first carefully filtering out the unwanted signals. Moreover, the current at the input power port of the reaction

wheel can be easily related to the different operational modes due to the changes its waveform.

The setup is complemented with the dc supply that powers the reaction wheel and a line impedance stabilization network (LISN) employed to fix the impedance at the power port and to filter out conducted disturbances the auxiliary power supply might produce.

C. In-Band Time-Domain Analysis

Having the complete B-field waveform available is advantageous because it allows us to complement the reaction wheel characterization with in-band interference analysis. Hence, by applying digital bandpass filters, we can determine the portion of the EMI that disturb receive bands used for communication systems or sensitive instruments without considering outband emissions.

Furthermore, as the full magnetic flux vector is measured synchronously, the field orientation can be obtained and studied at any time. We analyze how the azimuth and elevation of the B-field changes according to the different functional modes measured or events. This analysis is performed by bandpass filtering the field at specific center frequencies for identifying different electromagnetic emissions sources based on the orientation of the B-field vector. Certain frequency bands are expected to be associated with the intrinsic movement of the reaction wheel rotor and others by other sources like connection cables.

Likewise, tailor-made in-band EMI detectors offering statistical information can be calculated. Based on the empirical data, the probability density function (pdf), the cumulative distribution function (CDF), and other statistical features could be computed for any parameter of the B-field. For example, the amplitude APD, or the extreme values might be of interest. Statistical detectors are useful for assessing the likelihood that an electromagnetic disturbance exceeds certain condition or violates a given threshold defined on either the time or the frequency domain. In particular, in [15] it was demonstrated how the APD detector is related to the performance of radio receivers.

III. EXPERIMENT

The measurements were conducted within a full anechoic chamber (FAC) at ESA-ESTEC. Although most of the external sources of electromagnetic noise were significantly attenuated by the shielding of the FAC, the contribution from the earth's magnetic field and those generated due to 50 Hz currents and its harmonics are still present. With the reaction wheel inside the FAC, the B-field probe and the current probe are connected as explained in Section II-B.

Other relevant settings used for this experiment are related to the total measured time and also to the probes specifications. The waveform record length was equivalent to 40 s per channel. This allowed to capture full cycles of the different functional modes in a single acquisition. With respect to the specifications of the probes, they have a flat response in the useful frequency range. For the current probe the conversion factor is 1 V per
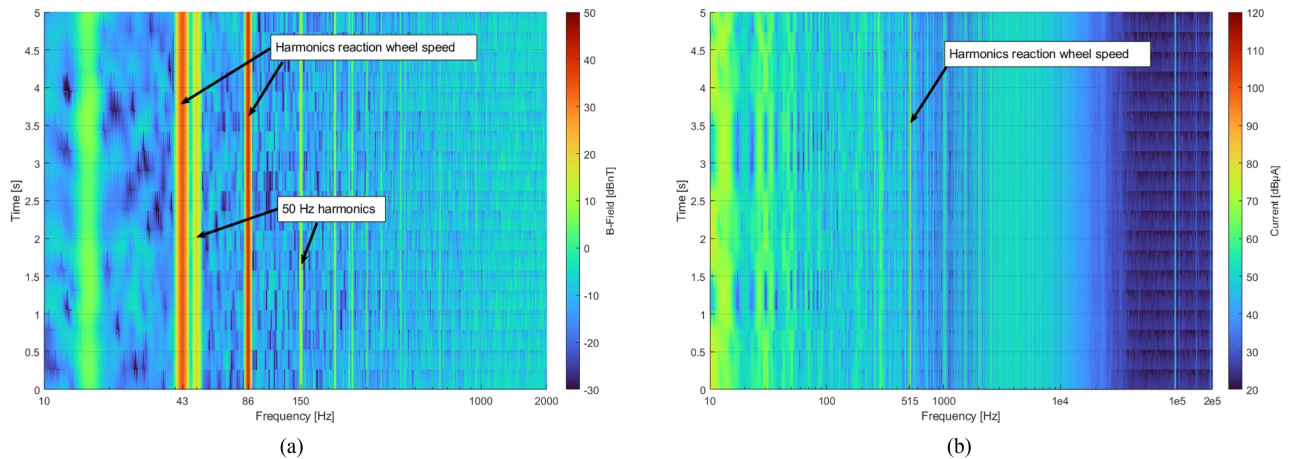
Fig. 3.   Spectrograms for steady-state, functional Mode A. (a) B-field. (b) Current.

10 A, and for the magnetic density flux probe conversion factor is 0.1 V per 1 μT.

A description of the EUT and of the functional modes considered as part of the experiment are provided in what follows.

A. Equipment Under Test

The reaction wheel used in the test campaign is MSCIs MicroWheel 4000 series. It is a torque actuator and momentum storage device with a maximum storage of up to 4 Nms. The nominal speed range is +/−5250 r/min (+/−550 rd/s), which is equivalent to 87.5 Hz. Maximum nominal torque that can be applied to the wheel is about 100 mNm. Basically, a reaction wheel is composed by a rotor, an stator and a fly wheel which produces the movement of the spacecraft. The reaction wheel under study has six slots, two for each phase A, B, and C, and four poles (two pairs) at the rotor.

B. Functional Modes

Commonly, reaction wheels are evaluated in constant speed mode. In such condition, no torque is applied to the wheel but there is a magnetic field due to the intrinsic movement of the rotor. Based on the operation of the reaction wheel, different predefined functional modes are defined in order to perform the worst-case emission assessment.

1) Mode A: Steady state. The reaction wheel is set to a constant speed of 270 rd/s, equivalent to 43 Hz. In this functional mode, the consumption of the device under test should be minimum and no ac contribution other from motor movement shall appear.
2) Mode B: Acceleration. In this functional mode the speed of the reaction wheel is modified from 0 rd/s up to 550 rd/s (0–87.5 Hz) applying a maximum torque of 100 mNm. With this torque set, the total time employed to reach the maximum speed is approximately 40 s.
3) Mode C: Deceleration. This functional mode is the opposite to the acceleration case using the same torque of 100 mNm. This time the reaction wheel starts at maximum

speed (550 rd/s) and decelerates till 0 rd/s in approximately 40 s.
4) Mode D: Short time speed modification. This mode is changing the speed between 270 rd/s (43 Hz) and 275 rd/s (43.8 Hz) using a maximum torque of 100 mNm. The acceleration and deceleration events last half a second and the interval between each acceleration or deceleration is 1.5 s. This functional mode imitates small corrections that constantly can occur during a mission and the probability to have it is high.

IV. RESULTS

A. Time-Frequency Domain Analysis

The first block of results corresponds to spectrograms obtained for each operating mode, intending to comprehend the performance of the reaction wheel and find out the worst-cases. For the steady-state (Mode A), two continuous frequency components are observed at 43 and 86 Hz as shown in Fig. 3. The 43 Hz component corresponds to the rotation speed of the rotor (270 rd/s), and the 86 Hz is its second harmonic. On the other hand, there is no remarkable frequency at the current spectrogram for Mode A because the current consumption is very low.

During acceleration (Mode B), Fig. 4, the two main frequencies components increase with time up to 87.5 and 175 Hz, which corresponds to the maximum speed of 550 rd/s and its second harmonic. The maximum speed is reached after 38 s, then the reaction wheel turns to steady-state without consuming current. In the acceleration's current spectrogram, the spectral content varies and stops when the wheel reaches the maximum speed at 38 s. The highest peak of the current follows the B-field, and it relates to the speed by a factor of 12; details can be found in Table I, where the reaction wheel speed, the two maximum B-field frequencies (Freq.1 and Freq.2), the frequency peak of current, and the ratio between current peak frequency and the wheel speed are listed. According to previous studies to understand the reaction wheel performance [3], the higher frequencies observed in the B-field spectrum are related to the speed of
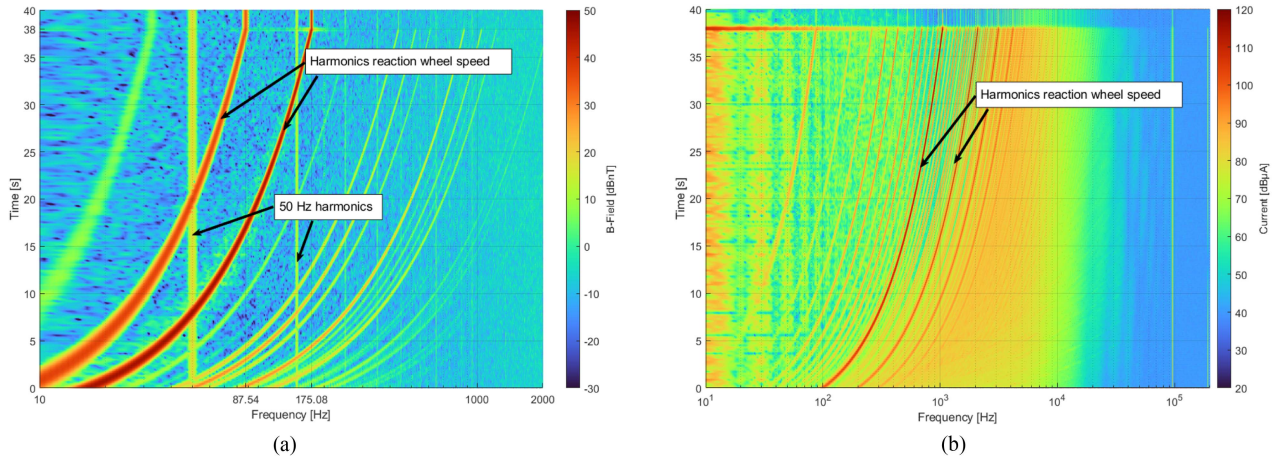
Fig. 4. Spectrograms for acceleration, functional Mode B. (a) B-field. (b) Current.
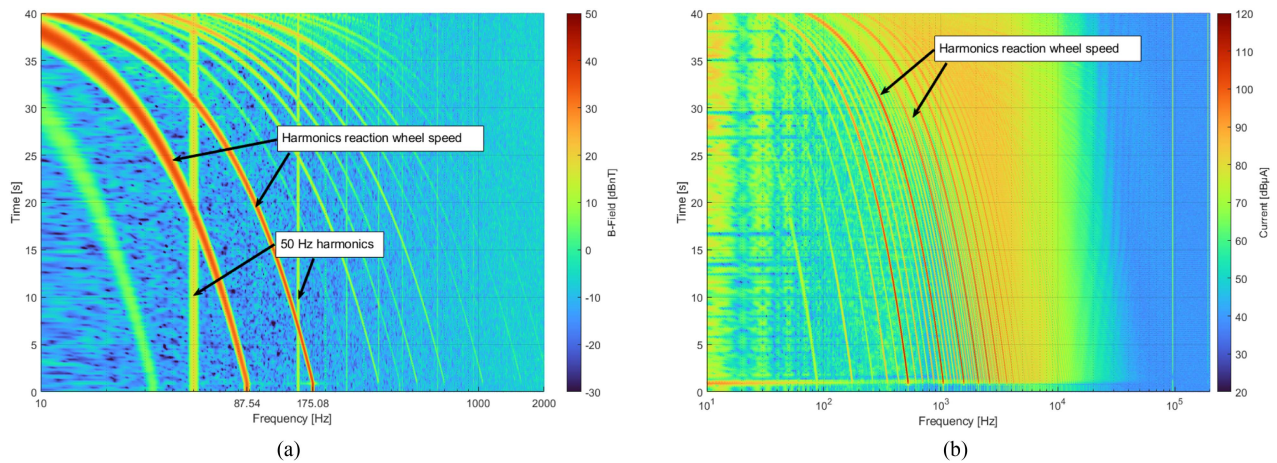

Fig. 5. Spectrograms for deceleration, functional Mode C. (a) B-field. (b) Current.

TABLE I
SPEED FREQUENCY AND ASSOCIATED PEAK FREQUENCIES FOR THE B-FIELD
AND THE CURRENT MEASUREMENT

Speed		B-field peaks		Current peaks	Ratio
rad/s	Hz	Freq. 1 [Hz]	Freq. 2 [Hz]	[Hz]	Peak/Speed
50	7.96	8	16	95.5	12.00
270	42.97	43	86	515.75	11.99
275	43.77	43.75	87.5	525	12.00
550	87.54	87.5	175	1050	12.00

the reaction wheel and the number of poles. Complementary, the most significant contributions are from the third and fifth harmonic.

The spectrogram obtained during deceleration (Mode C), Fig. 5, is a mirror of the acceleration one. For this operating mode, the B-field spectrogram has the prominent two peaks related to the maximum rotation speed at the beginning of the measurement, and they decrease in frequency to 0 Hz at the end of the measurement time (40 s).

Finally, in Fig. 6, for the short time speed modification case, noticeable peaks are observed on the B-field spectrogram, and

high emissions are produced on the current. Regarding the B-field, the peaks shift close to 43 and 87 Hz, because the speed varies slightly between 270 rd/s (43 Hz) and 275 rd/s (43.77 Hz). At the current spectrogram, the highest emissions are produced during the acceleration, but not for all the frequency range. It is observable that some high-level dots appear on some occasions for other functional modes like the deceleration.

To find the component of the B-field causing the highest emissions, we compute its spectrum using a 1 Hz RBW for the acceleration and deceleration modes in the three different axes. The results are presented in Fig. 7, where emission components are observed up to 1 kHz. There is a stair behavior up to 175 Hz as this is the harmonic at the maximum speed achieved. During the acceleration, the emissions are higher, and the component with the maximum B-field is the *x*-axis.

Once the highest component has been identified, we compute the B-field and the current spectrum for the four operational modes (see Figs. 8 and 9, respectively) to view the spectral differences and maximum values with a higher resolution. For example, for Mode A (steady-state), although the wheel turns without significant current, the peak level at 43 and 86 Hz
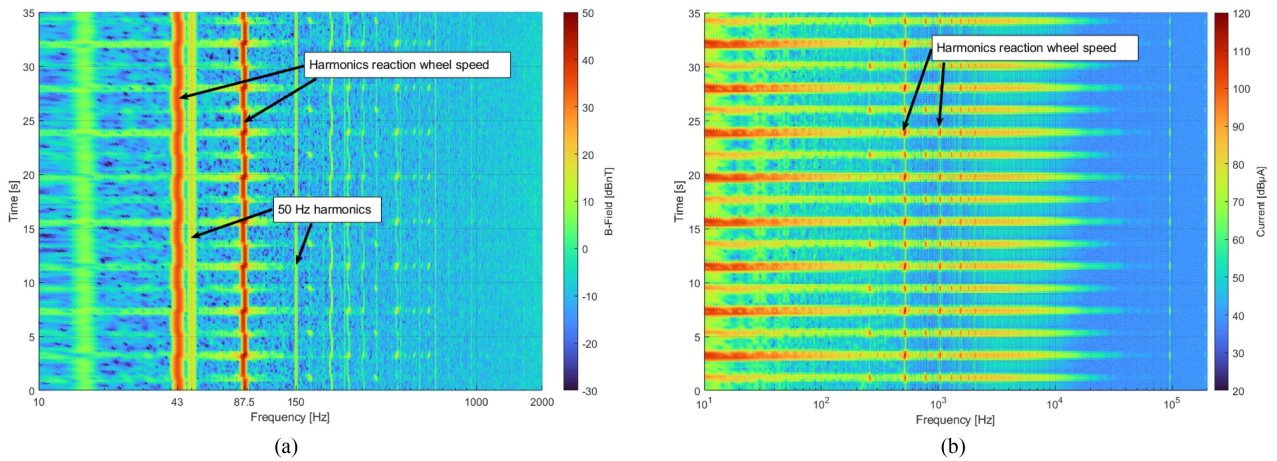
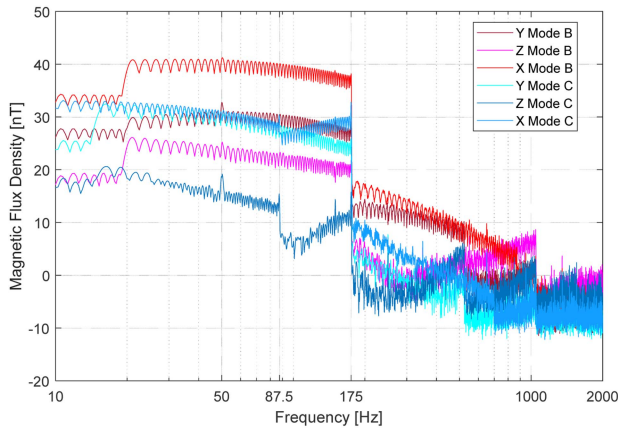Fig. 6.　Spectrograms for short acceleration and deceleration, functional Mode D. (a) B-field. (b) Current.

Fig. 7.　Spectrum of the magnetic flux density for functional Mode B (acceleration) and functional Mode C (deceleration). The B-field's x-, y-, and z-components are displayed for both operational modes when the speed varies from 0 to 87.54 Hz.
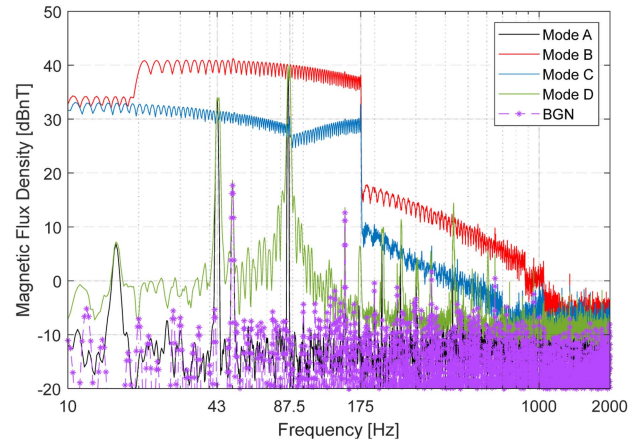

Fig. 8.　Spectral measurements for B-field x-component for functional mode cases A, B, C, and D.

Fig. 9.　Spectral measurements for current for functional mode cases A, B, C, and D.

is comparable to the other functional modes. Contrarily, at the current spectrum, Fig. 9, the prominent peaks of the the current spectrum associated with the movement in steady-state mode are 35 dB lower than in other functional modes.

For the acceleration case (Mode B), the maximum peak of the B-field appears between 20 and 175 Hz as the rotor changes the speed. Alternatively, in Fig. 9, where the spectrum of the current is computed, it is observed that this functional mode is the one causing a higher level of emissions at all the frequency bands.

In deceleration, the performance of the B-field and the current spectrum are similar to the one during acceleration. Nevertheless, the magnitude of the magnetic flux density and the current is lower than the functional acceleration mode. For instance, the x-component of the magnetic flux is 10 dB lower than in the acceleration, considering the higher emissions of the frequency range. Furthermore, although the current spectrum is higher than the steady-state case, the deceleration mode produces lower emissions on the B-field at the fundamental frequency and the second harmonic.
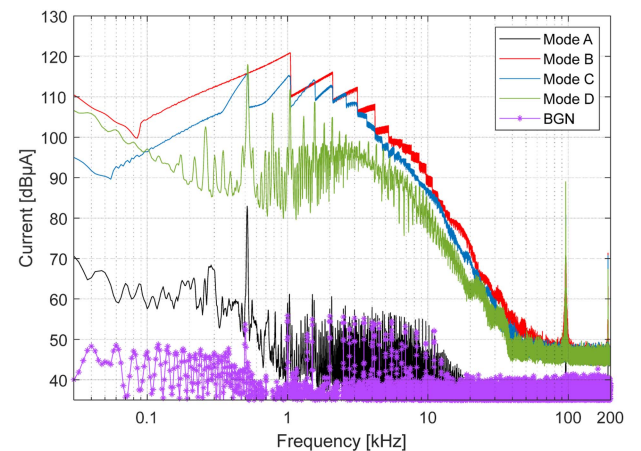
Finally, functional mode D is evaluated, where slight acceleration and deceleration are produced at the reaction wheel. This case is comparable to the acceleration or steady-state case for the B-field, the worst case. Nevertheless, we see a double
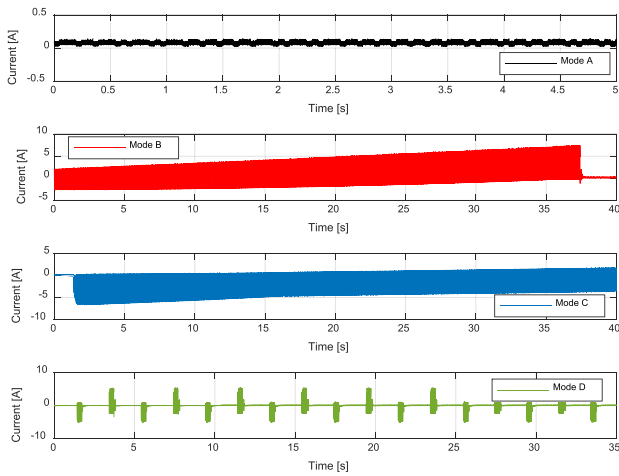
Fig. 10.   Current time-domain data for functional modes A, B, C, and D.
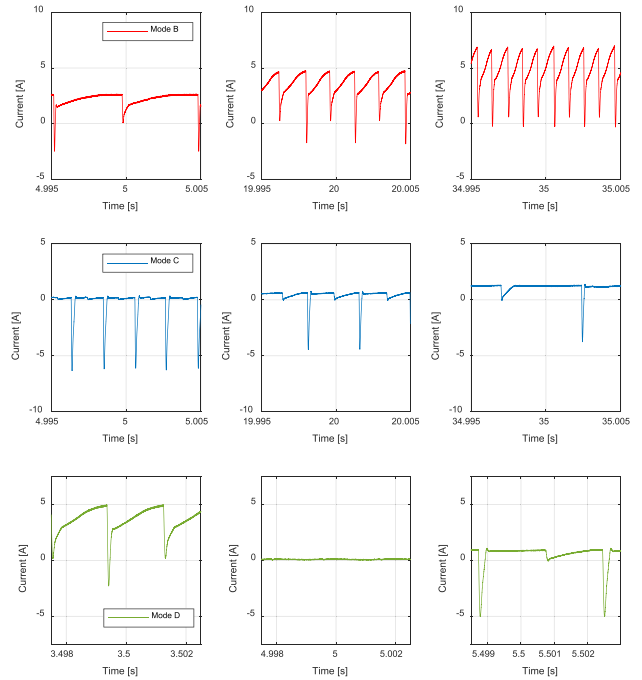

Fig. 11.   Zoom view of the current time-domain data for functional modes B, C, and D.

Fig. 12.   Zoom view of the time-domain data for current and B-field x-component for functional Mode D.

peak close to 87.5 Hz, which can be related with small speed change in the reaction wheel. On the other hand, if the D operational mode is compared with the steady-state, we see higher harmonics and more broadband interference, as in the steady-state, the only observable interference is related to the speed of the wheel and the second harmonic. This performance can be explained in the current signal spectrum, where the level of the harmonics and the broadband behavior is observed. This broadband performance close to the main peak implies that the acceleration case is worse than the steady-state if a wider resolution bandwidth is employed. For instance, if the 87.5 Hz peak is computed with an RBW of 10 Hz instead of 1 Hz, the value for the acceleration is 8 dB higher than the steady state.

Therefore, measuring the emissions only while the reaction wheel is steady-state is not representative enough for characterizing its emissions, especially if we consider that worst-case with slight speed changes in real missions can occur often.

To complement the analysis, evaluating the time-domain signal of the current is essential because the current changes for every mode. In Fig. 10, for mode A, the steady-state, the current value is lower than 0.25 A, and nonimportant variations are observed. On the other hand, the maximum current value increases during the acceleration and drops drastically when the full speed is reached. If we zoom the view at three different times, 5, 20, and 35 s, in Fig. 11, we see the changes in the amplitude and shape of the current signal. As we increase the speed, the time between the observable peaks is reduced. Alternatively, for the deceleration case, the frequency is reduced as the measurement time is incremented, which is related to the speed of the reaction wheel. As a result, the magnitude of the current ripples and the observable sine-wave is reduced. Therefore, the reduction on the measured B-field is comprehensible. Finally, we have a mixture of modes for the short acceleration and deceleration case, mode D. According to the relationship shown in Table I between the rotor speed and the B-field measured, the highest peak is modified between 86 and 87.5 Hz. Hence, we can
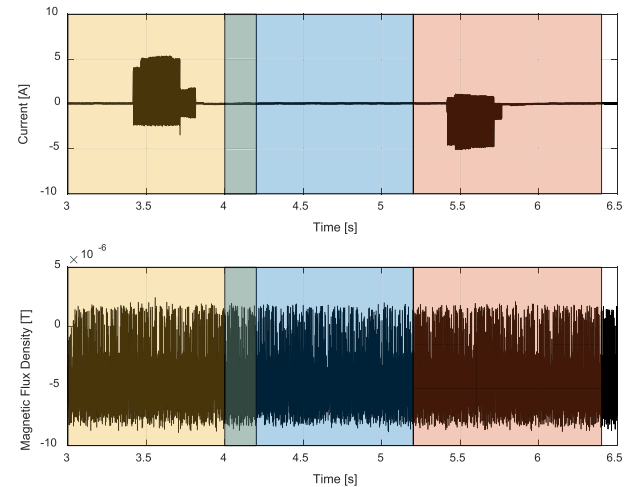
identify all functional modes from the current waveform and use the waveforms to correlate current and B-field measurements.

If we employ only the recorded data for the short event functional mode, mode D, we can correlate all the acceleration, deceleration, or steady-state with the current consumption. If we directly evaluate the raw B-field time-domain data from the envelope, unfortunately, we cannot appreciate any change between the different events occurring at the operating mode D. Fortunately, as the synchronized current measurement is available, we can use it to identify the three different types of events in mode D, time-gating the signal, and computing again the spectrum. From the graph in Fig. 12, we decide to split the
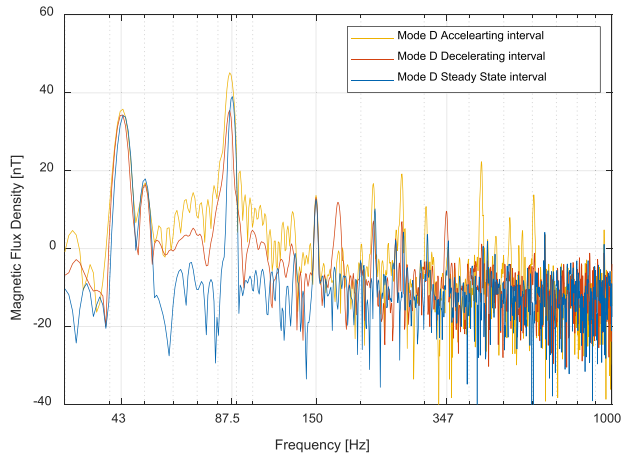
Fig. 13. Spectral measurements for B-field x-component for the different measurement instants in functional Mode D.
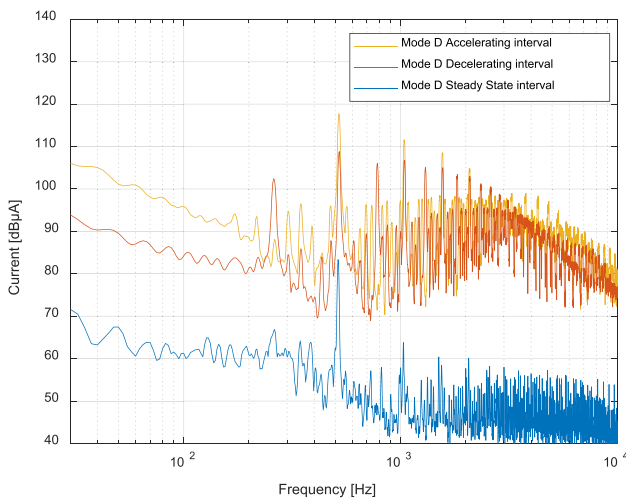

Fig. 14. Spectrum measurements for current for the different measurement instants in functional Mode D.
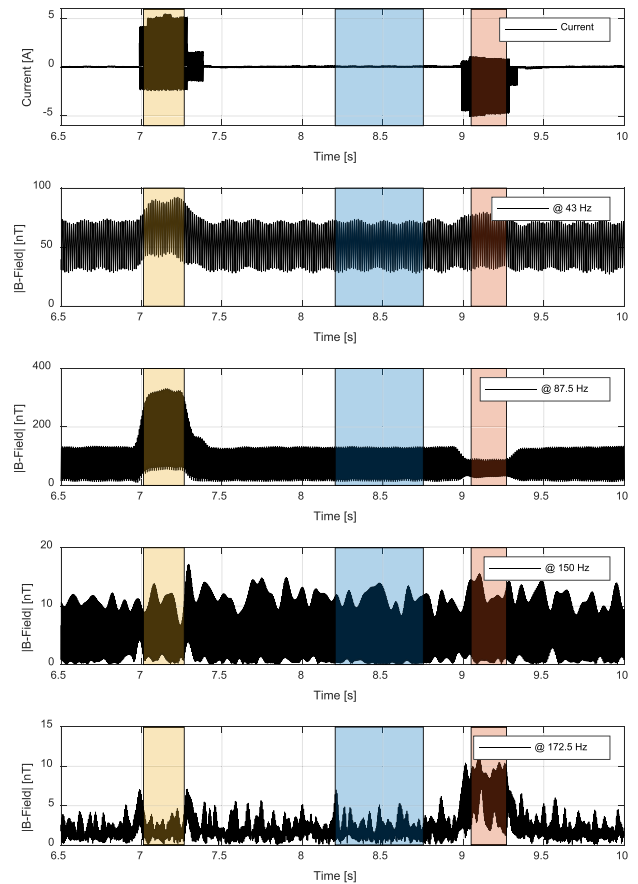

Fig. 15. Time-domain data for functional mode D filtering at key frequencies. The B-field module has been obtained considering the three-axis components.

On the other hand, the current spectrum presented in Fig. 14 shows that when the speed is constant, the spectral content is low and is a best-case regarding the emissions. Otherwise, when acceleration is present, we have the highest level of emissions, but again in some frequencies, the worst case is deceleration.

B. In-Band Time-Domain Evaluation

Once the different critic frequencies have been identified, we can filter the B-field considering the three-axis components at the selected frequency bands. For example, in Fig. 15, the current time-domain data is related to the B-field filtering the interference at 43, 87.5, 150, and 172.5 Hz. When we filter the B-field at 43 Hz slight amplitude variations appear for the 87.5 Hz response. We observe the correlation with the specific events; the lowest emission is during the deceleration, the highest during the acceleration, and the steady-state. On the contrary, the 172.5 Hz filtered B-field shows that the deceleration is causing the highest emission, even higher than the acceleration. The explanation for the differences between features is unknown because we do not have enough information about the reaction wheel construction. Still, the data are helpful for the B-field disambiguation between operational modes. Finally, the events cannot correlate with a significant B-field change for the EMI

B-field signal in interval 1, between 3 and 4.2 s for acceleration (yellow box), between 4 and 5.2 s for steady-state (blue box), and between 5.2 and 6.4 s for deceleration (red box). Then, the field and current spectrums are presented in Figs. 13 and 14 using an RBW equal to 3 Hz for the B-field and 10 Hz for the current.

The results of the B-field are comparable to the ones presented before for mode A, mode B, and mode C. Nevertheless, the emissions related to the movement of the reaction wheel are limited to the speeds of 270 and 275 rd/s. On this occasion, the emissions occupy a limited frequency range, with the maximum peak levels at 86 and 87.5 Hz. Like the previous analysis, the worst-case scenario appears to be the acceleration event, but we can highlight that all the different modes are close to the fundamental frequency and the second harmonic. Additionally, the worst case is during the deceleration at specific frequencies, for example, at 172.5 or 347 Hz, we see the highest emission level for the B-field when the reaction wheel is reducing the speed.
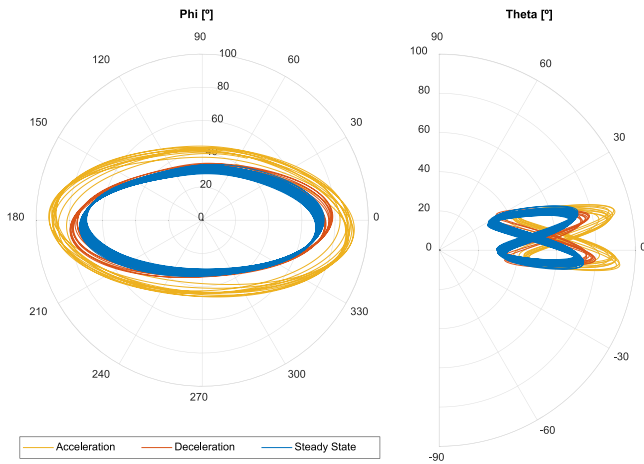
Fig. 16. B-field vector trajectory in nanotesla when the EMI is filtered at 43 Hz frequency band.
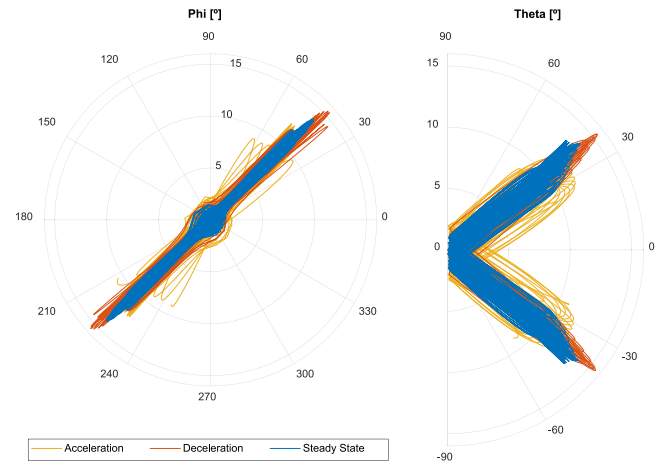

Fig. 18. B-field vector trajectory in nanotesla when the EMI is filtered at 150 Hz frequency band.
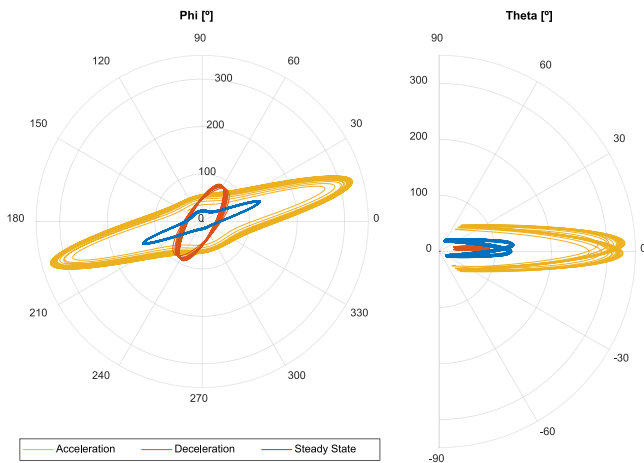

Fig. 17. B-field vector trajectory in nanotesla when the EMI is filtered at 87.5 Hz frequency band.
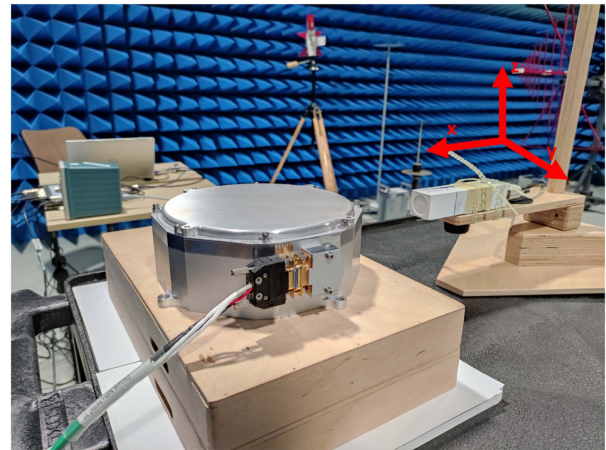

Fig. 19. Picture of the test set-up conducting measurements on the reaction wheel.

filtered at 150 Hz. Therefore, thanks to the postprocessing and the synchronized current measurements, we can obtain the B-field identifying worst cases considering interesting frequency bands.

Moreover, suppose we combine the event identification, the bandpass filtering, and the three-axis components. In that case, we also have the opportunity to calculate the orientation of the magnetic field for the Mode D. Hence, using the x-, y-, and z-components that can be correlated with the acceleration, deceleration, and steady-state events by current observation, we compute the B-field at 43, 87.5, and 150 Hz. Figs. 16–18 show the B-field orientation using polar coordinates, where ϕ represents the azimuth and θ the elevation of the field vector. The B-field in spherical coordinates has been computed by transforming the cartesian measurements according to the axis reference in Fig. 19. We have selected the 43 Hz frequency associated with the reaction wheel's movement according to the speed. Otherwise, the 87.5 Hz is selected as this is the highest value observed at the B-field spectrum in Fig. 13. Finally, the 150 Hz frequency is selected because it is a harmonic of 50 Hz, so it is expected to have a different radiating pattern compared to the previously selected cases.

In Fig. 16, we observe the vector trajectory of the B-field associated with the rotation of the reaction wheel (i.e., 43 Hz). The B-field varies in the time domain, pointing to different directions according to the movement and changing the level related to the event computed. The diagram shows that the highest emission is found during the reaction wheel's acceleration, and the steady-state is slightly lower than the deceleration. Nevertheless, the rotation of the field vector remain the same for the three different modes.

On the other hand, if the emissions for 87.5 Hz presented in Fig. 17 are studied, the trajectory of the B-field vector change strongly for the different modes. Opposite to the previous frequency evaluation, the B-field pattern is distinct for the acceleration, deceleration, and steady-state. We can highlight the absolute difference between acceleration and deceleration. Moreover, the B-field level is significantly different while in acceleration mode, which is the highest one by a large margin.

Regarding the study at 150 Hz, a noticeable different behavior is observed. The results presented in Fig. 18 show that the three different modes exhibit the same response in terms of their B-field trajectory. The field orientation only varies mainly between 45° and 225° for the azimuth and between 40° and
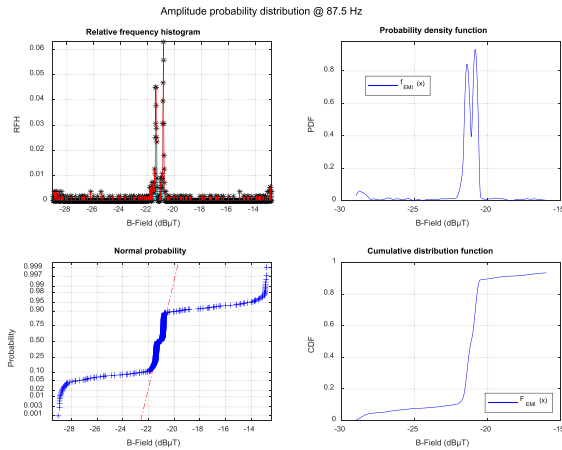
Fig. 20.   Statistical data for functional mode D at 87.5 Hz.

$-40°$ in elevation. Therefore, it is clear that the reaction wheel structure is not radiating the B-field corresponding to the third harmonic of the 50 Hz mains frequency. Instead, the source of the magnetic field can be one of the cables inside the FAC, which matches in orientation with the B-field pattern observed in Fig. 18. Hence, this further postprocessing enables the user to find out the direction and the source of the magnetic field.

Finally, statistical analysis can provide meaningful information for mission purposes, even though this is not commonly used as part of EMC assessment. Specific interference statistics have been computed for mode D to highlight the possibility of correlating the data with risk mitigation. For example, in Fig. 20, we can observe the pdf, the cumulative density function (CDF), the relative frequency histogram, and the normal probability plot when the time-domain data for the x-component is filtered at 87.5 Hz. For instance, from the pdf, two peak values are observed with high probabilities, meaning that the amplitude of the interference mainly varies between those levels, but it is possible to have higher or lower values between -30 and -15 dB μT. Otherwise, in the CDF diagram, we see the probability that the interference has a specific value of amplitude or less. The APD diagram is obtained directly from the CDF, and it can be related, for instance, to the performance of digital communication systems. Although the protection of communication systems is not in the scope of this study, this can be used in the future with the data available, or the probabilistic information can provide us with sufficient data to protect other critical systems like scientific mission instrumentation.

This type of analysis is potentially significant as it is possible to compute any other useful output for future missions without the need to conduct another measurement campaign.

V. Conclusion

The multichannel multidomain methodology implemented was useful for identifying the worst-case in terms of magnetic field emissions. It became clear that it would not be valid to test the reaction wheel solely in steady-state operating mode. This is because, worst cases occur in dynamic operating modes each of them having its own spectral signature. Particularly, slight speed changes can produce the highest level of EMI, being the acceleration the worst-case in general. However, for specific

frequency bands the deceleration generates the maximum value for the B-field.

The synchronous monitoring of the current enables the user to identify the different functional modes and correlate them with their magnetic field emissions or other construction characteristics like the number of poles or size. Moreover, the EMC assessment can be performed during the test campaign or afterward because recording the time-domain data enables the user to modify spectrum parameters or carry out advanced postprocessing. The study presented in this article demonstrates that the different events produced in the functional mode D can be easily recognized, allowing us to calculate the spectrum for each type of event, filter the B-field at any critical frequency band, or obtain complementary statistical information. Furthermore, we have seen that the synchronized measurement of the three-axis B-field can be used to evaluate the B-field vector trajectories, and see how they change to derive the source of the EMI. Nevertheless, other possibilities like the extrapolation of the magnetic field at other distances can be contemplated in the future [19]. This approach is particularly interesting for space applications that use very sensitive magnetic field instrumentation, and the B-field should be extrapolated from measurements performed close to the EUT.

Therefore, a new standard procedure to characterize the reaction wheels or other critical spacecraft elements shall be further investigated. The procedure should store synchronous the time-domain data to link the current consumption with the magnetic field generated. Furthermore, creating a database can provide information for future missions without the need to perform a measurement campaign again, determining beforehand the possibility to use specific reaction wheels according to the mission requirements. Moreover, this laboratory data can be used for in-mission data cleaning, as the current can be monitored during the missions, and the magnetic field generated can be correlated with the current measurement. Hence, some data can be discarded or corrected according to the characterization studies performed in-lab with the reaction wheels for future missions or already launched ones.

References

[1] K. Dang, P. Narvaez, J. Berman, K. Pham, and A. Curiel, "Magnetic shielding concepts for reaction wheel assembly on nasa europa clipper spacecraft," in *Proc. IEEE Int. Symp. Electromagn. Compat. Signal/Power Integrity*, 2020, pp. 305–311.

[2] M. Pudney et al., "Advances in reaction wheel design for magnetic cleanliness," in *Proc. ESA Workshop Aerosp. EMC*, 2019, pp. 1–6.

[3] A. Nicolai et al., "Towards a magnetically clean reaction wheel with active magnetic field mitigation," in *Proc. ESA Workshop Aerosp. EMC*, 2019, pp. 1–6.

[4] P. Brown et al., "Meeting the magnetic EMC challenges for the in-situ field measurements on the juice mission," in *Proc. ESA Workshop Aerosp. EMC*, 2019, pp. 1–6.

[5] A. Junge and F. Marliani, "Prediction of dc magnetic fields for magnetic cleanliness on spacecraft," in *Proc. IEEE Int. Symp. Electromagn. Compat.*, 2011, pp. 834–839.

[6] R. J. Perez and P. S. Narvaez, *DC Magnetic Cleanliness Description for Spaceflight Programs*, 2019, pp. 621–672.

[7] S. T. Spantideas and C. N. Capsalis, "Reaction wheel modeling for static and low-frequency magnetic cleanliness requirements," *IEEE Trans. Electromagn. Compat.*, vol. 63, no. 5, pp. 1609–1612, Oct. 2021.

[8] S.-D. J. Kakarakis, S. T. Spantideas, N. C. Kapsalis, C. N. Capsalis, and A. Junge, "A software-based calibration technique for characterizing the magnetic signature of EUTs in measuring facilities," *IEEE Trans. Electromagn. Compat.*, vol. 59, no. 2, pp. 334–341, Apr. 2017.
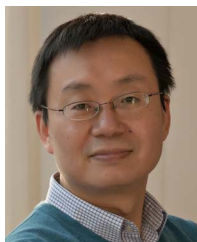
[9] M. A. Azpúrua, J. A. Oliva, M. Pous, and F. Silva, "Fast and automated verification of multi-channel full time-domain EMI measurement systems," in *Proc. IEEE Int. Instrum. Meas. Technol. Conf.*, 2017, pp. 1–6.

[10] M. Pous, M. A. Azpúrua, J. A. Oliva, M. Aragón, I. González, and F. Silva, "Full time domain emi measurement system applied to railway emissions according to IEC 62236-3-1/en 50121-3-1 standards," in *Proc. Int. Symp. Electromagn. Compat.*, 2018, pp. 260–265.

[11] M. A. Azpúrua, M. Pous, and F. Silva, "Statistical evaluation of measurement accuracy in full time-domain EMI measurement systems," in *Proc. Int. Symp. Electromagn. Compat.*, 2020, pp. 1–6.

[12] M. Pous, M. Azpúrua, and F. Silva, "Benefits of full time-domain emi measurements for large fixed installation," in *Proc. Int. Symp. Electromagn. Compat.*, 2016, pp. 514–519.

[13] M. A. Azpúrua, M. Pous, and F. Silva, "Specifying the waveforms for the calibration of CISPR 16-1-1 measuring receivers," *IEEE Trans. Electromagn. Compat.*, vol. 62, no. 3, pp. 654–662, Jun. 2020.

[14] M. A. Azpúrua, M. Pous, M. Fernandez, and F. Silva, "Dynamic performance evaluation of full time-domain EMI measurement systems," in *Proc. Int. Symp. Electromagn. Compat.*, 2018, pp. 561–566.

[15] M. Pous, M. A. Azpúrua, and F. Silva, "Measurement and evaluation techniques to estimate the degradation produced by the radiated transients interference to the GSM system," *IEEE Trans. Electromagn. Compat.*, vol. 57, no. 6, pp. 1382–1390, Dec. 2015.

[16] K. Wiklundh, "Relation between the amplitude probability distribution of an interfering signal and its impact on digital radio receivers," *IEEE Trans. Electromagn. Compat.*, vol. 48, no. 3, pp. 537–544, Aug. 2006.

[17] M. A. Azpúrua, M. Pous, J. A. Oliva, B. Pinter, M. Hudlička, and F. Silva, "Waveform approach for assessing conformity of CISPR 16-1-1 measuring receivers," *IEEE Trans. Instrum. Meas.*, vol. 67, no. 5, pp. 1187–1198, May 2018.

[18] M. A. Azpúrua, M. Pous, S. Çakir, M. Çetinta, and F. Silva, "Improving time-domain EMI measurements through digital signal processing," *IEEE Electromagn. Compat. Mag.*, vol. 4, no. 2, pp. 82–91, 2nd Quarter 2015.

[19] C. Trenkel, S. Engelke, K. Bubeck, J. Lange, Z. Tenacci, and A. Junge, "Reliable distance scaling of ac magnetic fields for space mission verification campaigns," in *Proc. ESA Workshop Aerosp. EMC*, 2019, pp. 1–9.

Marco A. Azpúrua (Senior Member, IEEE) received the B.Sc. degree in telecommunications engineering in 2008 and the M.Sc. degree in electrical engineering from the Universidad Central de Venezuela, Caracas, Venezuela, in 2013, and the Ph.D. degree in electronics engineering from the Universitat Politécnica de Catalunya (UPC), Barcelona, Spain, in 2018 for his contributions to Full Time-Domain EMI measurements and their applications in complex scenarios.

Currently, he is working as an Associate Professor with the Electronic Engineering Department, UPC, where he is part of the Research Staff with the Electromagnetic Compatibility Group (GCEM). Moreover, he is the Cofounder of EMC Barcelona, a start-up company. His research interests include electromagnetic compatibility, antenna and microwave measurement technologies, estimation of measurement uncertainty in complex test systems, and validation methods.

Dr. Azpúrua is a Fellow of the StandICT.eu 2023 project and a Member of the CISPR/CIS/B/WG 1 & WG 7, the IEEE EMC and IMS societies, and the International Committee on Electromagnetic Safety. He was the recipient of the IEEE Instrumentation and Measurement Society Faculty Course Development Award in 2020, the UPC Special Doctoral Award for the Best Thesis in the field of Electronics (2017–2018 academic year), and the Best Symposium Student Paper Award in the 2017 EMC Europe International Symposium on Electromagnetic Compatibility.

Teodor Bozhanov (Member, IEEE) received the masters degree in aerospace engineering from the University of Manchester, Manchester, U.K., in 2018.

He has performed multiple system studies mainly in the aerospace area and has a broad range of experience in multiple engineering domains. For the past year years, he has been working as a Systems Engineer for the Proba-3 Project at ESA, ESTEC. Currently, he is mainly occupied with the validation and testing of the flight software, as well as hardware testing on system, and equipment level.

Marc Pous (Member, IEEE) received the M.Sc. degree in telecommunications engineering and the Ph.D. degree in electronics engineering from Universitat Politécnica de Catalunya, Barcelona, Spain, in 2009 and 2015, respectively.

From 2003 to 2006, he was with the Department of Electromagnetic Compatibility, LGAI Technological Centre, Barcelona, Spain. In 2006, he joined the Electromagnetic Compatibility Group, Universitat Politécnica de Catalunya, where he has been participating in international and national research projects related to the automotive, aerospace, railway, and medical industries. He is also Cofounder of EMC Barcelona startup. In December 2022 he joined HE SPACE OPERATIONS BV working for ESA, European Space Agency. His research interests include the development of novel time-domain interference measurement techniques and new evaluation methods to overcome not properly measured disturbances following the harmonized electromagnetic compatibility standards.

Dr. Pous is a Member of the International Steering Committee (ISC) EMC Europe, the Vice-Chairman of EMC Europe 2019, Barcelona, and the Treasurer of the IEEE Electromagnetic Compatibility Society Spanish chapter.

Ferran Silva (Senior Member, IEEE) received the M.Sc. degree in telecommunication engineering and the Ph.D. degree in electronics engineering from the Universitat Politécnica de Catalunya (UPC), Barcelona, Spain, in 1989 and 1997, respectively.

He is currently an Associate Professor with the Department of Electronic Engineering, UPC. Since 1993, he has been the Head of the Electromagnetic Compatibility Group, GCEM-UPC. His research interests include electromagnetic compatibility (EMC) in near field and time domain, with application to transport, medical and industrial areas.

Dr. Silva has made more than 140 publications about EMC in journals, conferences, and books. He has participated in 32 research projects related to EMC. He is a Senior Member of the IEEE EMC Society and has been the Chair of the Spanish Chapter of the same society in two different periods. He is also a Member of the EMC Spanish Standardization Committees SCTC77-210 and the CTN208 SCCISPR210 A. He was the Chairman in 2006 and 2019 of the EMC Europe International Symposium editions in Barcelona. Since 2021, he has been chairing the EMC Europe International Steering Committee.

Dongsheng Zhao (Senior Member, IEEE) received the Ph.D. degree in electrical engineering from the Technical University of Delft, Delft, The Netherlands, in 2009.

In 2008, he joined the R&D Department, VSL, Dutch Metrology Institute as a Research Scientist. He served as a project coordinator, project leader in several international research projects covering EMC test methods, EM Field and SAR measurements, solid state lighting, power and energy measurement, ultrafast electronics characterization, and Quantum voltage standard. In 2017, he joined the RHEA System B.V. and working for European Space Agency. He is now a Senior EMC Engineer and Deputy EMC Laboratory Manager. He was and is involved in more than 20 projects, including SMILE, SatAIS, ROSE-L, ALTIUS, JUICE, ATHENA projects.

Johannes Wolf (Senior Member, IEEE) received the diploma (M.Sc.) and Ph.D. degrees in electrical engineering from the University of Technology, Dresden, Germany, in 1988 and 1994, respectively.

In 1999, he joined industry - Kayser-Threde GmbH, Munich, Germany, as a System Engineer, working on several projects for the European Space Agency (ESA). Since 2001, he has been working with the EMC section of the Electrical Department, European Space Technology Center (ESTEC), European Space Agency (ESA) in Noordwijk, Netherlands and providing EMC support to projects from Science, Earth observation, Navigation, human spaceflight, and robotic exploration as well as for Launchers. Since 2014, he has been the Head of the EMC section. Starting form March 2022, he is working as a Senior Advisor EMC, ESA ESTEC. His research interests include EMC, in particular ESD, powerline communication (on dc lines), experimental procedures, and setups for EMC testing.